Two closely related structure types with unprecedented bioctahedral rare-earth-metal clusters centered by transition metals: A(2)R(10)I(17)Z(2) (A=Rb,Cs; R=La,Ce,Pr; Z=Co,Ni,Ru,Os)...

4 AUTHORS, INCLUDING:

James Martin
North Carolina State University
105 PUBLICATIONS **1,631** CITATIONS

SEE PROFILE

Laura Hoistad Strauss
University of Northern Iowa
38 PUBLICATIONS **173** CITATIONS

SEE PROFILE

Two Closely Related Structure Types with Unprecedented Bioctahedral Rare-Earth-Metal Clusters Centered by Transition Metals: $A_2R_{10}I_{17}Z_2$ (A = Rb, Cs; R = La, Ce, Pr; Z = Co, Ni, Ru, Os) and $La_{10}I_{15}Os_2$

Michael Lulei, James D. Martin, Laura M. Hoistad, and John D. Corbett*

Contribution from the Department of Chemistry, Iowa State University, Ames, Iowa 50011

Abstract: A family of compounds has been discovered in which pairs of octahedral rare-earth-metal clusters, each centered by a late transition metal Z, share a common edge. These $R_{10}Z_2$ units, sheathed and interbridged by iodine atoms, occur in the quaternary phases $Rb_2La_{10}I_{17}Co_2$, $Cs_2La_{10}I_{17}Z_2$ (Z = Co, Ni, Ru, Os), $Cs_2Ce_{10}I_{17}Os_2$, and $Cs_2Pr_{10}I_{17}Z_2$ (Z = Co, Ru, Os) and in the ternary $La_{10}I_{15}Os_2$. All are obtained as black, air-sensitive crystals from reactions of RI_3, R, Z, and RbI or CsI as appropriate in welded Nb containers at 800−850 °C. The structure of $Cs_2Ce_{10}I_{17}Os_2$ has been refined by single-crystal X-ray diffraction methods for comparison with the isotypic $Cs_2La_{10}I_{17}Co_2$ (monoclinic, $C2/m$, $Z = 2$, $R(F)/R_w = 4.0/4.4\%$), and the structure of a unique ternary $La_{10}I_{15}Os_2$ has been defined (triclinic, $P\bar{1}$, $Z = 1$, $R/R_w = 5.0/5.1\%$). These new bioctahedral clusters may be regarded as the missing links between discrete clusters and infinite chains of condensed octahedral clusters among rare-earth-metal cluster halides that are stabilized by interstitial transition metals. The biclusters in both structures are extensively interconnected into three-dimensional arrays through bridging iodine atoms. The structural interconversion between $Cs_2La_{10}I_{17}Os_2$ and $La_{10}I_{15}Os_2 + 2CsI$ may be easily visualized in terms of changes in iodide bridging modes and accommodation of cesium cations. All the biclusters contain an odd number of cluster-bonding electrons, and this feature has been confirmed by magnetic susceptibility studies. EHMO cluster and band calculations on biclusters and their structures are in agreement with the localized bonding properties and ranges of electron counts.

Introduction

Reduced rare-earth-metal cluster halides have been extensively studied since their discovery around 25 years ago. Since then a great variety of compounds have been discovered through exploratory synthesis guided by some knowledge of electronic and structural principles.[1−3] The great majority of their structures are constructed from rare-earth-metal octahedra R_6 that contain a mandatory interstitial atom Z and are bridged over all edges by halide atoms to form the well-known $R_6X_{12}Z$ units (X = Cl, Br, I). The interstitial atoms provide not only central bonding within the clusters but also additional valence electrons that aid in fulfilling certain minimal electron counts necessary for metal−metal and metal−interstitial bonding with these relatively electron-poor metals.[4] The interstitial atoms may be late transition metals from all three periods (i.e., group 7−11 elements), second-period main-group elements (B−N), or even C_2 units. The clusters within these compounds are isolated from each other and interconnected into 3-D frameworks only via the bridging halide atoms, for example in $Y_6I_{10}Ru$.[5] The X:R stoichiometry ratios of the ternary compounds remain fairly low, ≤12:7 in order to achieve closed-shell clusters with the above Z and such relatively electron-poor host metals. Another large, well investigated group of compounds are more reduced and structurally comprised of condensed infinite chains of edge-

sharing metal octahedra that are similarly centered by interstitial atoms and bridged over the open edges by halides, as in the structure of Pr_4I_5Ru for instance.[6]

Despite intensive exploration, oligomeric intermediates between the discrete clusters and infinite cluster chains are still relatively rare. In the few examples, compounds such as $Y_{16}I_{20}Ru_4$, $Y_{16}Br_{24}Ir_4$, and $Gd_{20}I_{28}Mn_4$ have more spherical metal arrays that can be derived by tetrahedral condensation of four R_6 octahedra as their outstanding structural feature.[2,7−9] In addition, there are a number of ternary gadolinium phases such as $Gd_{10}Cl_{17}C_4$ and, more recently, $CsEr_{10}I_{18}C_4$ and $Cs_3Tb_{10}Cl_{21}C_4$ in which pairs of rare-earth-metal octahedra share a common edge.[10−14] So far these bioctahedral clusters are known exclusively with acetylidic (ethynidic) C_2 as the interstitial unit and only for the smaller rare-earth metals (Y, Gd, Tb, Er).

Our continued search for the "missing links" in the chemistry of reduced rare-earth-metal cluster compounds stabilized by transition metals has recently been successful in two ways. One, as has been briefly communicated,[15] is the discovery of

[⊗] Abstract published in *Advance ACS Abstracts,* January 1, 1997.

(1) Corbett J. D. In *Modern Perspectives in Inorganic Crystal Chemistry;* Parthé, E., Ed.; Kluwer Academic Publishers: Dordrecht, The Netherlands, 1992; p 27.

(2) Corbett, J. D. *J. Alloys Compd.* **1995**, *224*, 10.

(3) Simon, A.; Mattausch, Hj.; Miller, G. J.; Bauhofer, W.; Kremer, R. K. In *Handbook on the Physics and Chemistry of Rare Earths;* Gschneidner, K. A., Jr., Eyring, L., Eds.; Elsevier Science Publishers B. V.: New York, 1991; Vol. 15, p 191.

(4) Hughbanks, T. *Prog. Solid State Chem.* **1989**, *19*, 329.

(5) Hughbanks, T.; Corbett, J. D. *Inorg. Chem.* **1989**, *28*, 631.

(6) Payne, M. W.; Dorhout, P. K.; Corbett, J. D. *Inorg. Chem.* **1991**, *30*, 1467.

(7) Payne, M. W.; Ebihara, M.; Corbett, J. D. *Angew. Chem., Int. Ed. Engl.* **1991**, *30*, 856.

(8) Ebihara, M.; Martin, J. D.; Corbett, J. D. *Inorg. Chem.* **1994**, *33*, 2079.

(9) Steinwand, S. J.; Corbett, J. D. *Inorg. Chem.* In press.

(10) Simon, A. *Angew. Chem., Int. Ed. Engl.* **1981**, *20*, 1.

(11) Warkentin, E.; Masse, R.; Simon, A. *Z. Anorg. Allg. Chem.* **1982**, *491*, 323.

(12) Artelt, H. M.; Meyer, G. *Z. Anorg. Allg. Chem.* **1994**, *620*, 1527.

(13) Uhrlandt, St.; Artelt H. M.; Meyer, G. *Z. Anorg. Allg. Chem.* **1994**, *620*, 1532.

(14) Hinz, D. J.; Meyer, G. *Z. Kristallogr.* **1995**, *210*, 957, 958.

(15) Lulei, M.; Maggard, P. A.; Corbett, J. D. *Angew. Chem., Int. Ed. Engl.* **1996**, *35*, 1704.

Table 1. Lattice Parameters of Quaternary Compounds $A_2R_{10}I_{17}Z_2$ with Bioctahedral Clusters (Monoclinic, Space Group $C2/m$)[a]

compd	N[b]	a	b	c	β	V
$Rb_2La_{10}I_{17}Co_2$	37	13.853(4)	18.997(5)	9.890(3)	95.92(3)	2589(1)
$Cs_2La_{10}I_{17}Co_2$	40	13.865(5)	18.986(5)	9.887(3)	96.00(3)	2588(1)
$Cs_2La_{10}I_{17}Ni_2$	52	13.933(2)	18.912(2)	9.966(1)	96.63(1)	2608.6(6)
$Cs_2La_{10}I_{17}Ru_2$	52	13.884(3)	19.074(6)	10.007(3)	95.81(2)	2636(1)
$Cs_2La_{10}I_{17}Os_2$	21	13.892(4)	19.025(5)	9.982(4)	95.33(2)	2627(2)
$Cs_2Ce_{10}I_{17}Os_2$	61	13.771(3)	18.826(3)	9.939(2)	96.00(2)	2562.5(8)
$Cs_2Pr_{10}I_{17}Co_2$	45	13.647(3)	18.704(4)	9.764(1)	95.99(1)	2478.6(8)
$Cs_2Pr_{10}I_{17}Ru_2$	42	13.679(3)	18.683(3)	9.879(2)	96.10(1)	2510.5(8)
$Cs_2Pr_{10}I_{17}Os_2$	47	13.703(4)	18.722(7)	9.894(4)	96.23(3)	2524(2)

[a] From Guinier powder diffraction data at 22 °C with Si as an internal standard, $\lambda = 1.540562$ Å. [b] The number of indexed reflections employed in the least-squares refinement.

$Cs_2La_{10}I_{17}Co_2$, in which a bioctahedral La_{10} cluster is centered by Co atoms. Subsequent experiments have shown that this compound is not a singularity but representative of a family, and we have now established a range of workable R metal hosts and transition-metal interstitials Z as well as some physical properties. A second example reported here is the so-far unique example of a bioctahedral cluster in a ternary compound, $La_{10}I_{15}Os_2$, with a structure that can be readily related to that of $Cs_2La_{10}I_{17}Co_2$, etc. Both types are novel as all of the biclusters contain an odd number of electrons, and we have also gained some further understanding of the bonding in these compounds through measurements of magnetic susceptibilities and EHMO calculations on both the clusters and the three-dimensional solids.

Experimental Section

Syntheses. All of the syntheses were performed by reaction of certain rare-earth metals R, rare-earth-metal triiodides RI_3,[5] alkali-metal iodides AI or potassium, and transition elements Z. The rare-earth metals La, Ce, and Pr (Ames Laboratory, 99.99%), potassium (Baker, 99.9%, under Ar), and the transition metals Co, Ni, Ru, and Os (Johnson-Matthey, >99.9%) were used as received. NaI, KI, RbI, and CsI (Alfa, 99.9%) were dried by slow heating under dynamic high vacuum and then sublimed. Because most of the reagents and all of the products are very sensitive to air and, especially, moisture, all operations were carried out in N_2-filled gloveboxes with typical humidity levels less than 0.1 ppm (volume). The general reaction techniques in welded Nb tubing have been described elsewhere.[16] Mixtures with an overall stoichiometry $A_2R_{10}I_{17}Z_2$ were heated at 800 °C for ~27 days and cooled at 5 °C h^{-1} to 300 °C, and then the furnace was turned off. The products were black crystals of the new phases in high yields (>80%) besides ca. 10% each of ROI and CsI or RbI. The ubiquitous ROI formation is presumably caused by adventitious sources, i.e., water slowly evolving from the fused silica jacket during the heating process or contamination of the highly moisture-sensitive rare-earth-metal triiodides during their storage in the glovebox. Reactions with NaI or CaI_2 as cation sources most often yielded only the corresponding $R_7I_{12}Z$ cluster phases[1] while KI gave primarily K_2LaI_5 (below). Addition of NaI (~10%) to parallel CsI reactions was found to increase the crystallinity of the $Cs_2R_{10}I_{17}Z_2$ phases. This most likely acted as a flux (melting point: 661 °C) as NaI was still present at the end of the reaction. Reactions with Z = Mn and Fe yielded $CsR_6I_{10}Z$,[17] while those run with other neighboring interstitial prospects yielded unidentified microcrystalline phases.

$La_{10}I_{15}Os_2$ was obtained as 80% of the products of reactions loaded with the overall stoichiometry $K_2La_6I_{12}Os$ (with K metal) and run at 850 °C. The powder pattern also showed ~20% of the normal-valent lanthanum compound K_2LaI_5.[18] The latter has often been observed after reactions with K, La, and I components, especially when no reduced product was obtained and irrespective of the transition metal present as a potential interstitial. Attempts to synthesize $La_{10}I_{15}Os_2$

(or other) without additional K have not been successful so far, and we presume that K_2LaI_5 (or other) is a necessary flux component.

X-ray powder patterns of samples mounted in an airtight assembly between pieces of cellophane were collected with the aid of an Enraf-Nonius Guinier camera, Cu Kα radiation ($\lambda = 1.540562$ Å), and with Si introduced as an internal standard. Lattice constants of known phases were obtained by least-squares refinements of 21 to 61 lines that were read from the Guinier films by an automatic scanner (LS-20, KEJ Instruments, Stockholm) and indexed on the bases of the model patterns calculated from single-crystal structural data (below). Lattice parameters for the new quaternary phases are listed in Table 1. In all cases, powder patterns calculated on the basis of the refined structure agreed very well with the observed ones. All yields were estimated according to the relative intensities of the powder pattern lines for each phase present.

Single-Crystal X-ray Studies. (a) $Cs_2Ce_{10}I_{17}Os_2$. Black, block-like crystals (~0.05 × 0.07 × 0.1 mm³) of this phase were mounted in thin-walled capillaries in the glovebox, and their quality was checked by Laue and oscillation photographs on Weissenberg cameras. The initial monoclinic cell parameters and the orientation matrices were obtained from a least-squares refinement of the setting angles of 25 centered reflections that were collected on an Enraf-Nonius CAD4 diffractometer with the aid of graphite-monochromated Mo Kα radiation. A total of 2435 reflections were measured ($2\theta \leq 50°$; $-h$, $+k$, $\pm l$ at room temperature), and these gave 1389 unique data ($I > 3\sigma_I$) for the space group $C2/m$ after averaging redundant data ($R_{avg} = 0.048$). The structural refinement started with the atom positions for $Cs_2La_{10}I_{17}Co_2$ as the powder pattern made this connection clear. Programs, scattering factors, etc. utilized were those in the instrument package TEXSAN.[19] An empirical absorption correction was first applied to the full data set with the aid of four Ψ-scans and later, to improve the correction ($\mu = 253$ cm^{-1}), by DIFABS on the results from isotropic refinement, as recommended[20] (min/max relative transmission: 0.880/1.329). The residuals after the anisotropic refinement of all atoms (83 variables) were $R(F) = 0.040$ and $R_w = 0.044$. The largest residual peak was 1.98 e/Å³, 2.30 Å from I1. Some data collection and refinement parameters are given in Table 2. This solution allowed accurate indexing of the powder pattern and a better determination of the lattice constants, and the latter were in turn used for all distance calculations. The final atomic coordinates, isotropic-equivalent temperature factors, and their estimated standard deviations are listed in Table 3.

(b) $La_{10}I_{15}Os_2$. The procedures for selecting crystals of $La_{10}I_{15}Os_2$ and the determination of the orientation matrices were the same as described for $Cs_2Ce_{10}I_{17}Os_2$. A total of 4407 data at $2\theta \leq 50°$, $\pm h$, $\pm k$, $+l$ were collected at room temperature with the aid of a Siemens P4 Diffractometer on a irregular, black crystal (ca. 0.1 × 0.1 × 0.08 mm³) and gave 1779 unique data ($I > 3\sigma_I$, $R_{avg} = 0.062$) in the space group $P\bar{1}$. The structure was solved using direct methods (SHELXS[21]). The data were corrected empirically for absorption with the aid of the average of six Ψ-scans (minimum transmission: 0.667). The residuals after anisotropic refinement were $R(F) = 0.050$ and $R_w = 0.051$ (125

(16) Corbett, J. D. *Inorg. Synth.* **1983**, *22*, 15, 31.

(17) Lulei, M.; Corbett, J. D. *Z. Anorg. Allg. Chem.* **1996**, *622*, 1677.

(18) Meyer, G.; Soose, J.; Moritz, A.; Vitt, V.; Holljes, Th. *Z. Anorg. Allg. Chem.* **1985**, *521*, 161.

(19) TEXSAN, version 6.0, Molecular Structure Corp., The Woodlands, TX, 1990.

(20) Walker, N.; Stuart, D. *Acta Crystallogr.* **1983**, *A39*, 159.

(21) Sheldrick, G. M. SHELXS-86. Göttingen University, Germany, 1986.

Table 2. Selected Crystal and Refinement Data for $Cs_2Ce_{10}I_{17}Os_2$ and $La_{10}I_{15}Os_2$

	$Cs_2Ce_{10}I_{17}Os_2$	$La_{10}I_{15}Os_2$
space group, Z	$C2/m$ (No. 12), 2	$P\bar{1}$ (No. 2), 1
lattice constants (Å, deg)		
a	13.771(3)	10.049(3)
b	18.826(3)	11.035(3)
c	9.939(2)	11.778(3)
α	90	91.90(3)
β	96.00(2)	114.15(3)
γ	90	110.63(3)
V (Å³)	2562.5(8)	1091(1)
μ(Mo Kα), cm⁻¹	253.1	266.0
rel transm range	0.880−1.329	0.667−1.000
R,[a]	4.0	5.0
R_w,[b] %	4.4	5.1

[a] $R = \sum||F_o| - |F_c||/\sum|F_o|$; $R_w = [\sum w(|F_o| - |F_c|)^2/\sum w(F_o)^2]^{1/2}$; $w = \sigma_F^{-2}$.

Table 3. Positional and Isotropic Equivalent Displacement Parameters for $Cs_2Ce_{10}I_{17}Os_2$

atom	x	y	z	B_{eq}[a]
Ce1	0.1428(1)	0.34900(6)	0.4268(1)	1.28(4)
Ce2	0.1682(1)	0.0	0.4426(2)	0.99(7)
Ce3	0.0650(1)	0.5	0.6853(2)	1.13(7)
Ce4	0.2078(1)	0.5	0.1786(2)	1.08(7)
Cs	0.5	0.3257(2)	0.0	6.1(2)
I1	0.2097(2)	0.0	0.1304(2)	2.4(1)
I2	0.1394(1)	0.16930(8)	0.4198(2)	2.30(6)
I3	0.2178(1)	0.3316(1)	0.1370(1)	2.37(8)
I4	0.0620(2)	0.0	0.7194(2)	2.4(1)
I5	0.0745(1)	0.3252(1)	0.7271(1)	1.57(6)
I6	0.0	0.5	0.0	2.7(2)
Os	0.3580(1)	0.0	0.5705(2)	0.67(4)

[a] $B_{eq} = (8\pi^2/3)\sum_i\sum_j U_{ij}a_i^*a_j^*\vec{a}_i\vec{a}_j$.

Table 4. Positional and Isotropic Equivalent Displacement Parameters for $La_{10}I_{15}Os_2$

atom	x	y	z	B_{eq}
La1	0.2292(5)	0.5801(3)	0.0533(4)	1.1(1)
La2	0.3009(4)	0.9063(3)	0.2784(3)	1.13(9)
La3	0.0884(4)	0.5443(3)	0.3323(3)	1.3(1)
La4	0.8318(4)	0.7536(3)	0.1795(3)	1.2(1)
La5	0.9749(4)	0.7960(3)	0.9002(3)	1.5(1)
I1	0.3459(5)	0.4439(4)	0.3063(4)	1.6(1)
I2	0.2191(5)	0.7420(4)	0.8161(4)	1.3(1)
I3	0.1481(6)	0.3851(5)	0.5815(4)	2.9(2)
I4	0.3905(6)	0.7987(4)	0.5381(5)	2.7(1)
I5	0.2701(5)	0.0905(4)	0.0577(4)	1.7(1)
I6	0.5704(5)	0.8510(4)	0.2311(5)	2.7(2)
I7	0.0952(5)	0.0438(4)	0.3477(4)	1.7(1)
I8	0.5	0.5	0.0	3.1(3)
Os	0.0325(4)	0.6750(3)	0.1208(3)	0.72(5)

variables). The largest residual peak in the map was 2.47 e/Å³, 1.6 Å from La5 and 1.7 Å from I2. The final results are given in Table 4.

A larger summary of data collection and refinement information for $Cs_2Ce_{10}I_{17}Os_2$ and $La_{10}I_{15}Os_2$ as well as the anisotropic displacement parameters for all atoms are tabulated in Supporting Information. These and the F_o/F_c data are also available from J.D.C.

Magnetic Measurements. Samples of $Cs_2La_{10}I_{17}Ni_2$ (41 mg) and $Cs_2La_{10}I_{17}Os_2$ (48 mg) and selected ground single crystals of $La_{10}I_{15}Os_2$ (31 mg) were sealed within improved fused silica susceptibility containers[22] under He and then studied on a Quantum Design MPMS SQUID magnetometer. The magnetization of the first sample was checked as a function of applied field between 0 and 5.5 T at 100 and 250 K to screen for possible magnetic impurities such as unreacted Ni; the second phase was similarly studied at 150 and 250 K, and the third at 10, 50, 100 and 250 K. The Ni sample showed negligible

(22) Guloy, A. M.; Corbett, J. D. *Inorg. Chem.* **1996**, *35*, 4669.
(23) Payne, M. W.; Corbett, J. D. *Inorg. Chem.* **1990**, *29*, 2246.

impurities (M(T) → 0 at $H = 0$) while the two Os samples showed temperature-independent zero-field intercepts of ∼2 × 10⁻⁵ and 4.5 × 10⁻⁵ emu, respectively, from presumed ferromagnetic impurities, for which the magnetization data were accordingly corrected. Molar susceptibilities for all three samples were obtained at 3 T over the range of 6−300 K as well as for $La_{10}I_{15}Os_2$ at 1 T. Data were corrected for the susceptibility of the container and for the estimated core diamagnetism contributions, −1.17 × 10⁻³, −1.24 × 10⁻³, and −1.12 × 10⁻³ emu mol⁻¹, respectively.

Similar studies of a $Cs_2La_{10}I_{17}Co_2$ sample are not fully reported here. These showed a sizable content of an apparent ferromagnetic impurity in the sample, 8.5 × 10⁻⁴ emu, equivalent to 0.02% of the presumed elemental Co. However, the corrected data still gave a somewhat S-shaped fit to a generalized Curie-Weiss function and a μ value of ca. 1.7 μ_B.

Band Calculations. These were carried out[24] for both the isolated, iodine-sheathed ($La_6I_{12}Co)I_6^{6-}$ and ($La_{10}I_{18}Co_2)I_8^{11-}$ (the edge-bridged clusters with filled exo positions) and for the full bands of the primitive triclinic cells of $La_{10}I_{17}Co_2^{2-}$ and $La_{10}I_{15}Co_2$ over a general 64 k-point mesh. Suitable H_{ii} parameters were determined from a full charge iteration calculation on both La and Co, viz. (in eV), La: 6s, −6.56; 6p, −4.38; 5d, −7.52; Co: 4s, −6.14; 4p, −2.89; 3d, −8.29. The I values came from calculations on $Y_6I_{10}Ru$.[5] The band structure from calculations on $La_{10}I_{15}Co_2$ with the more reliable charge-interated values for Co was not significantly altered when reasonable parameters for Os were employed.

Results and Discussions

$Cs_2R_{10}I_{17}Z_2$ **Phases.** The unprecedented discovery of $Cs_2La_{10}I_{17}Co_2$ has been followed by the synthesis of eight more isostructural $A_2R_{10}I_{17}Z_2$ phases as black plate-like crystals, namely, those that incorporate A = Cs or Rb, R = La, Ce, or Pr and Z = Co, Ni, Ru, or Os in various combinations. The lattice parameters and cell volumes listed in Table 1 show the expected volume relationships La > Ce > Pr as well as Os > Ru > Ni > Co except in the first step with La. Even so, the Os−Ru differences with La and Pr are at the 4 and 7 σ levels, respectively, and as will be shown later, the dimensional proportions of the clusters also change with just R, possibly from matrix effects. Of course, the volumes reflect differences in intercluster bonding as well, not just those within the clusters. We have noted before that the R−Z distances themselves often do not follow simple measures of the sizes of Z either as metals or cations.[1,24] Finally, the change from Cs to Rb does not diminish the cell parameters significantly, evidently because of the relatively large distances between Cs and the surrounding iodine atoms in what must be a rather rigid anionic network (below). There is no reason to believe nonstoichiometry of any interstitial is a significant feature in these phases, particularly because of the generally high yields, invariant lattice constants for each, small B_{eq} values of the three refined examples, and the violence a vacancy would do electronically to the localized bonding within a bicluster (below).

The crystal structure of $Cs_2Ce_{10}I_{17}Os_2$ exhibits significant dimensional differences from that of the isotypic $Cs_2La_{10}I_{17}Co_2$, which has only been briefly described.[15] Distances in the two structures are compared in Table 5. As shown in Figure 1,[25] the most remarkable structural feature is the $Ce_{10}Os_2$ unit, a pair of octahedra that share a common Ce3−Ce3 edge and are each centered by an Os atom. The bicluster is noticeably unsymmetrical. In both the Co and Os compounds, the distances from the interstitial atom to the R2 and R4 vertices at the extremes of the common equatorial plane are less (∼0.15 Å)

(24) Band calculations were performed using the EHMACC suite of programs written at Cornell University by various members of the R. Hoffmann group.
(25) All structural drawings were produced with ATOMS, Shape Software, Kingsport, TN.

Table 5. Interatomic Distances (in Å) for $Cs_2R_{10}I_{17}Z_2$

atoms	$Cs_2La_{10}I_{17}Co_2$[a]	$Cs_2Ce_{10}I_{17}Os_2$	atoms	$Cs_2La_{10}I_{17}Co_2$	$Cs_2Ce_{10}I_{17}Os_2$
Z–R1 (×2)	2.885(1)	2.843(1)	I1–R2	3.221(2)	3.214(3)
Z–R2	2.779(3)	2.785(2)	I1–R3	3.461(2)	3.434(3)
Z–R3	2.794(3)	2.855(3)	I1–R4	3.395(2)	3.383(3)
Z–R3[b]	3.000(3)	2.957(2)			
Z–R4	2.659(3)	2.742(3)	I2–R1	3.254(2)	3.239(2)
(Z–R)ave	2.834	2.838	I2–R1	3.399(1)	3.384(2)
R1–R1[c]	4.405(2)	4.333(3)	I2–R2	3.242(1)	3.217(2)
R1–R2	4.019(1)	3.980(2)			
R1–R3[b]	4.024(1)	4.050(2)	I3–R1	3.192(1)	3.177(2)
R1–R3[b]	4.148(1)	4.104(2)	I3–R4	3.241(1)	3.202(2)
R1–R4	3.914(1)	3.928(2)			
R2–R3	4.011(2)	4.012(3)	I4–R2	3.275(2)	3.248(3)
R2–R4	3.951(2)	3.969(3)	I4–R2	3.404(2)	3.402(3)
R3–R3[d]	3.757(3)	3.923(4)	I4–R4	3.261(2)	3.226(3)
R3–R4	4.144(2)	4.124(3)			
			I5–R1	3.266(1)	3.246(2)
Cs–I1 (×2)	4.514(2)	4.473(4)	I5–R1	3.268(2)	3.253(2)
Cs–I2 (×2)	4.359(2)	4.407(2)	I5–R3	3.343(1)	3.318(2)
Cs–I3 (×2)	4.233(2)	4.251(2)			
Cs–I3 (×2)	4.383(2)	4.332(3)	I6–R3 (×2)	3.415(1)	3.342(2)
Cs–I4 (×2)	4.426(2)	4.447(4)	I6–R4 (×2)	3.212(2)	3.206(2)
Cs–I5 (×2)	4.144(2)	4.130(4)			
			Z–Z	4.416(5)	4.289(3)

[a] Reference 15. [b] Distance on the I6 side. [c] Distance between apex atoms. [d] Distance in the shared edge.
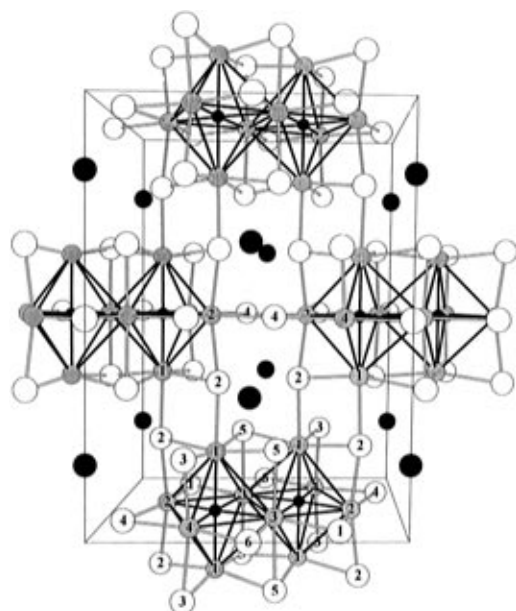
Figure 1. [001] perspective view of the structure and cell of $Cs_2Ce_{10}I_{17}Os_2$ with cerium positions defining the bioctahedra as gray and cesium as black spheres. Additional iodine bridging in the normal direction along $\vec{c}$ is not shown. ($\vec{b}$ is vertical.)

Figure 2. [010] view of the structure of $Cs_2Ce_{10}I_{17}Os_2$ normal to Figure 1, with Ce atoms shaded. All of the bridging iodine atoms shown (I1,4,6) are coplanar with Ce2,3,4, and the apices of the bioctahedron are Ce1; Os is not visible. (The a–c cell face is outlined.)

than those to either the apex R1 atoms of the octahedra or the R3 atoms that define the shared edge, and the differences are more pronounced in the $La_{10}Co_2$ cluster. Remarkably, the average R–Z distances in the two examples are indistinguishable. The similar apex–apex (R1–R1) and Z–Z separations between the condensed octahedra in both are 0.2–0.3 Å longer than the comparable waist edges of the bioctahedra (R2–R3, R3–R4). In other words, the Z are displaced away from the shared edge, and also somewhat laterally toward the R2–R3 edge that is bridged by I1.

The degree of distortion of the skewed bicluster can be judged in the [001] view around the a–b cell face in Figure 2, roughly normal to that in Figure 1. We judge the latter distortions to arise principally from the unsymmetric intercluster iodine bridging, as emphasized in the second figure. The biclusters are centrosymmetric ($2/m$) with an inversion center at the
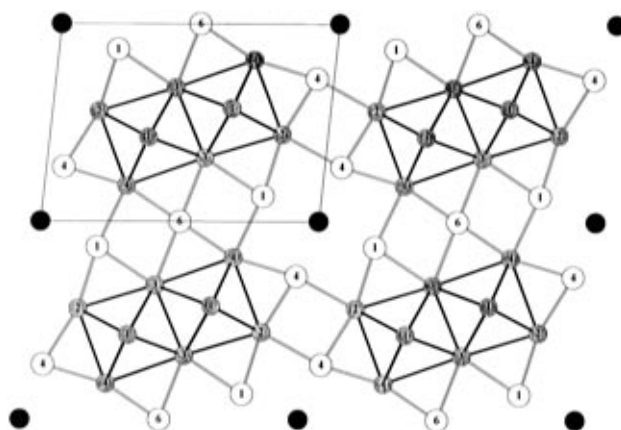
midpoint of the R3–R3 edge. The individual R–R distances around the $La_{10}Co_2$ and $Ce_{10}Os_2$ clusters are quite similar ($\Delta \leq 0.05$ Å) except for the shared R3–R3 edge which is, surprisingly, 0.166(5) Å shorter in $La_{10}Co_2$ with the smaller interstitial. This is accompanied by a 0.072(4) Å increase in the R1–R1 interoctahedral separation and a parallel 0.127(6) Å increase in d(Z–Z) with Co, changes that resemble a "breathing motion". Conversely, the larger transition metal Os and the smaller Ce (compared with Co and La) form a bioctahedron that is less distorted from its highest possible symmetry, D_{2h}.

All 22 edges of the $R_{10}Z_2$ bioctahedra in the $Cs_2R_{10}I_{17}Z_2$ structure are bridged by one of six crystallographically distinct iodine atoms which also in large part serve to connect the metal clusters into a three-dimensional network. As seen in Figure 2, pairs of I1 and I4 atoms centered about $(0,{}^1\!/_2,0)$ and $({}^1\!/_2,0,0)$ act as I^{i-a} (μ_3) to respectively bridge R2–R3 and R2–R4 edges and bond exo to I4 and I2 in adjoining clusters (I^{a-i}) and connect the clusters into layers. The μ_4-I6 atoms on the inversion center at $(0,{}^1\!/_2,0)$ are planar I^{i-i} and bridge R3–R4 edges in adjoining clusters into ribbons, in parallel with the above pairs of $I1^{i-a}$ bridges. These iodine atoms all lie in the mirror planes and so
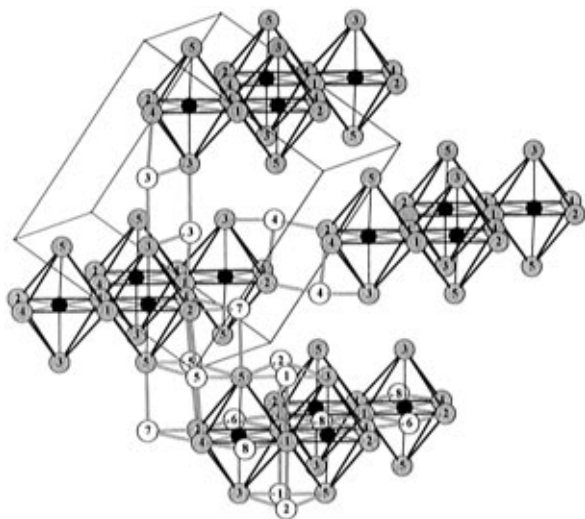
Figure 3. Off-[100] view of bioctahedra in $La_{10}I_{15}Os_2$ with La atoms shaded. (*c* lies approximately vertical.) Bridging along $\vec{a}$ is shown only for the bottom pair of clusters. Iodine atoms 3, 4, 6, and 7 bridge I^{i-a}, while 5 and 8 are I^{i-i} between clusters.

Table 6. Interatomic Distances (in Å) for $La_{10}I_{15}Os_2$

Os−La1	2.884(6)	I1−La1	3.349(5)	I6−La1	3.399(6)
Os−La1	3.006(4)	I1−La3	3.264(6)	I6−La2	3.223(6)
Os−La2	2.823(4)	I1−La5	3.233(5)	I6−La4	3.416(7)
Os−La3	2.878(5)				
Os−La4	2.762(5)	I2−La1	3.355(6)	I7−La2	3.278(6)
Os−La5	2.903(5)	I2−La3	3.305(5)	I7−La4	3.240(5)
		I2−La5	3.214(6)	I7−La5	3.422(5)
La1−La1[a]	3.910(8)				
La1−La2	4.060(6)	I3−La3	3.241(6)	I8−La1 (×2)	3.410(4)
La1−La3	4.058(5)	I3−La3	3.424(5)	I8−La4 (×2)	3.268(3)
La1−La3	4.163(5)	I3−La4	3.220(6)		
La1−La4	4.222(6)			Os−Os[b]	4.406(4)
La1−La5	4.033(5)	I4−La2	3.216(6)		
La1−La5	4.103(5)	I4−La2	3.438(5)		
La2−La3	4.028(5)	I4−La3	3.238(6)		
La2−La4	4.023(6)				
La2−La5	4.116(5)	I5−La2	3.324(5)		
La3−La4	3.988(5)	I5−La4	3.338(5)		
La3−La5[b]	4.268(6)	I5−La5	3.317(5)		
La4−La5	4.077(6)	I5−La5	3.333(5)		

[a] Distance in the shared edge. [b] Distance between the apex atoms.

their bonds to the R metal are all planar (and for I1 and I4, T-shaped, a fairly unusual configuration). Normal to these layers, Figure 1, μ_3-I2 atoms bond as I^{i-a} and I^{a-i} over the R1−R2 edges and link the clusters and layers along [010] at R1, again with nearly planar T-shaped bonding. The R1−R4 edges are covered by μ_2-I3 atoms (I^i) that form no bonds to neighboring clusters. Finally, two μ_3-I5 atoms as I^i each bridge a pair of R1−R3 edges in the saddle of the bioctahedron in a pyramidal manner. Therefore, the overall interconnection pattern of the iodine atoms can be succinctly formulated as $Cs_2(R_{10}Z_2)I^i_8I^{i-i}_{2/2}I^{i-a}_{8/2}I^{a-i}_{8/2}$. As expected, the R−I distances are a little shorter in the cesium member.

The Cs atoms are located within slightly distorted cuboctahedral iodine polyhedra defined by the framework of interbonded clusters. The Cs−I distances average to 4.34 Å in both $Cs_2La_{10}I_{17}Co_2$ and $Cs_2Ce_{10}I_{17}Os_2$. This is rather large compared with the crystal radius sum, 4.08 Å (CN 12),[26] especially when the presence of significant covalent bonding of the iodines to the rare-earth metals is considered. This contrast helps explain the relatively large isotropic temperature factor for Cs (~6 Å^2) as well as the fact that no difference in cell volume is found between $Cs_2La_{10}I_{17}Co_2$ and $Rb_2La_{10}I_{17}Co_2$ (Table 1). The large ellipsoid observed for Cs also parallels our experiences that large temperature factors are associated with poorly-bound alkali-metal atoms in other network compounds,[1] ~4.7 Å^2 in $Cs_4Pr_6I_{13}Os$[27] and 21 Å^2 in $KPr_6I_{10}Os$,[17] for instance. Obviously, the clusters and the bridging halides often build strong, dominant frameworks while the cations largely fulfill only charge requirements for the particular compounds.

$La_{10}I_{15}Os_2$. The closely related ternary compound $La_{10}I_{15}Os_2$ crystallizes in the form of irregular, black crystals. Because of the lower triclinic symmetry relative to the $A_2R_{10}I_{17}Z_2$ analogues, the bioctahedral unit is built from five crystallographically distinct La atoms and is only centrosymmetric. As seen in the side view in Figure 3, La1 atoms constitute the shared edge, La2 and La4 the vertices within the equatorial plane, and La3 and La5 the apical positions. The interatomic distances within this $La_{10}Os_2$ unit, Table 6, are quite comparable to those in $Cs_2Ce_{10}I_{17}Os_2$, with the lanthanum member

(26) Shannon, R. D. *Acta Crystallogr.* **1976**, *A32*, 752.
(27) Lulei, M.; Corbett, J. D. *Inorg. Chem.* **1996**, *35*, 4084.
(28) Lulei, M.; Martin, J. D.; Corbett, J. D. *J. Solid State Chem.* **1996**, *125*, 249.

showing 0.02 to 0.06 Å larger R−Z distances and a slightly greater cluster distortion. The unequal intercluster bridge bonding at the independent (La3, La5) apices in $La_{10}I_{15}Os_2$ produces increased distortion, but the shared edge remains effectively the same.

Because of the missing alkali-metal ions and the resulting lower I:La ratio, these clusters are more interconnected with a higher proportion of I^{i-i} bridges. The eight crystallographically-distinct iodine atoms link the clusters as follows: I1 and I2 are located above the saddles of the bioctahedra and simultaneously bridge the "inner" La1−La3 and La1−La5 edges in a pyramidal configuration (like I5 in $A_2R_{10}I_{17}Z_2$). Pairs of three-bonded I3, I4, I6, and I7 atoms related by inversion centers respectively cover the La3−La4, La2−La3, La1−La2, and La2−La4 edges and, as double-duty I^{i-a}, also form bonds to La3, La2, La4, and La5 atoms in adjacent clusters. The bonds at all of these are planar or nearly so except at I7 which is distinctly pyramidal. I5 atoms bridge La2−La5 and La4−La5 edges in adjacent clusters and hence exhibit I^{i-i} functionality in a pyramidal manner. And similar to I6 in the quaternary examples, I8 lies on an inversion center and covers pairs of La1−La4 edges on neighboring clusters as I^{i-i}, and its bonds are likewise coplanar. The interconnection pattern of the iodine atoms can therefore be summarized as $(R_{10}Z_2)I^i_4I^{i-i}_{6/2}I^{i-a}_{8/2}I^{a-i}_{8/2}$.

The centric pairwise arrangement of $I(5)^{i-i}$ and $I(7)^{i-a}$ bridges seen here about the origin is a familiar bridging mode, in this case between upper and lower faces at the ends of adjoining biclusters so as to generate the stair-step array or, alternately, a linear chain of canted clusters, Figure 3. A similar connectivity of clusters is found in linear chains in $Pr_6I_{10}Z$[5] and in bent chains in $KPr_6I_{10}Os$.[17] Figure 4 is a view normal to the horizontal direction in Figure 3 in which the bicluster on the left side is closer to the viewer. This also shows how in the stair-step arrangement biclusters interbridged by I5 and I7 are also joined side by side by the planar I6 (×2) and I8 bridges.

An electron count for the $La_{10}I_{15}Os_2$ phase ((10×3) − (15×1) + (2×8)) reveals that there are 31 electrons available for bonding within each bicluster. Interestingly, since there are two interstitial atoms per cluster and an odd number of iodine atoms in all of these compounds, it is impossible to achieve an even number of cluster-based electrons with only homoatomic interstitial elements. The three $A_2R_{10}I_{17}Co_2$ phases each have 33 cluster-based electrons available for metal−metal bonding, the nickel analogue has 35, and the five $Cs_2R_{10}I_{17}(Ru,Os)_2$ compounds have 31.
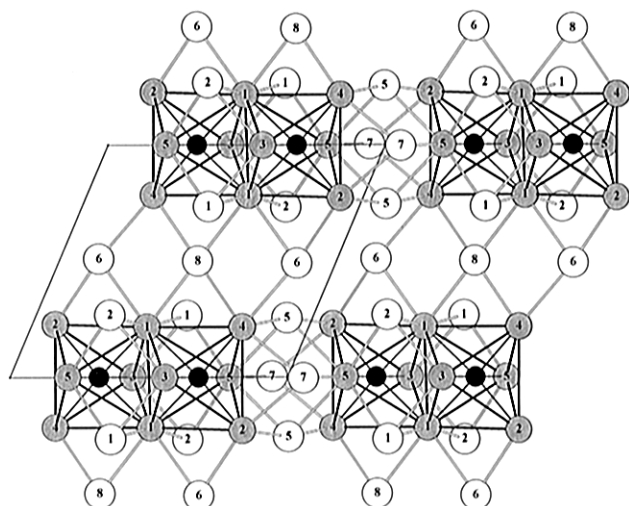
Figure 4. Approximate [00$\bar{1}$] view of the $La_{10}I_{15}Os_2$ structure, which is ca. normal to that in Figure 3, showing bridging within the horizontal stair-step bicluster chains and the coplanar bridges between chains along [100] (vertical). (The $a-b$ face of the cell is outlined.)

Structural Interrelationships. A surprisingly simple structural rearrangement can be visualized for the interconversion of these structure types via the reaction

$$La_{10}I_{15}Os_2 + 2CsI \rightleftharpoons Cs_2La_{10}I_{17}Os_2$$
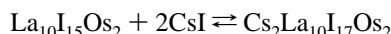
although we do not believe such a reaction would be feasible topotactically. Comparison of Figure 4 ($La_{10}I_{15}Os_2$) with Figure 2 ($Cs_2La_{10}I_{17}Os_2$) shows that the principal change in the network is the opening of the pairs of I(5)$^{i-i}$ bridges between each cluster pair in the former, replacing these by two pair of edge-bridging iodine atoms (I(3)^i and I(2)$^{i-a}$) in the product. This provides some room for the cations, and further expansion also occurs when the pair of I4-bridged clusters across the center of Figure 3 become coplanar so that I4 now bridges across La2−La4 edges in the waists of the biclusters, Figure 1. The I^{i-a} bridges by I7 between clusters at the dimer apices are reconstructed to free the new I4 atom (I7 in the $La_{10}I_{15}Os_2$) and to use I2, formerly part of I(5)$^{i-i}$ (above), as I^{i-a}. Comparison of Figure 3 with Figure 1 shows how the changes in I(4)$^{i-a}$ bridging in the latter require the biclusters to rotate about [001] as well while retaining the planar I6, I8 → I1, I6 connections that side-bridge these into ribbons (Figure 4 vs Figure 2). (These two views are not quite the same; Figure 4 shows the bridging between what become separate layers, while Figure 2 is of a single layer.)

The structures described here are of course related to those that contain the $Gd_{10}(C_2)_2$ biclusters. In all these compounds, the halides and the interstitial species, and the alkali-metal atoms as well in the $A_2R_{10}I_{17}Z_2$ cases, approximate cubic-close-packed arrays with the rare-earth metals in the octahedral holes. Indeed, the interconnection patterns of the halide atoms in $Cs_2La_{10}I_{17}Co_2$ and $Gd_{10}Cl_{17}C_4$[11] are similar, although the arrangement of the bioctahedral units with respect to each other is altered in the former in order to accommodate the large Cs atoms. This is also reflected by the higher symmetry of the present compound, $C2/m$ vs $P\bar{1}$.

Magnetic Properties. The odd electron counts for the La−Ni and the two La−Os biclusters and the calculational results to follow are nicely consistent with their magnetic susceptibility data. Those for $Cs_2La_{10}I_{17}Ni_2$, $Cs_2La_{10}I_{17}Os_2$, and $La_{10}I_{15}Os_2$ over 6−300 K are shown in Figure 5a−c, respectively. The data for the two osmium examples have been corrected for ferromagnetic impurities (see Experimental Section). The susceptibilities of all three are fit very well by the nonlinear
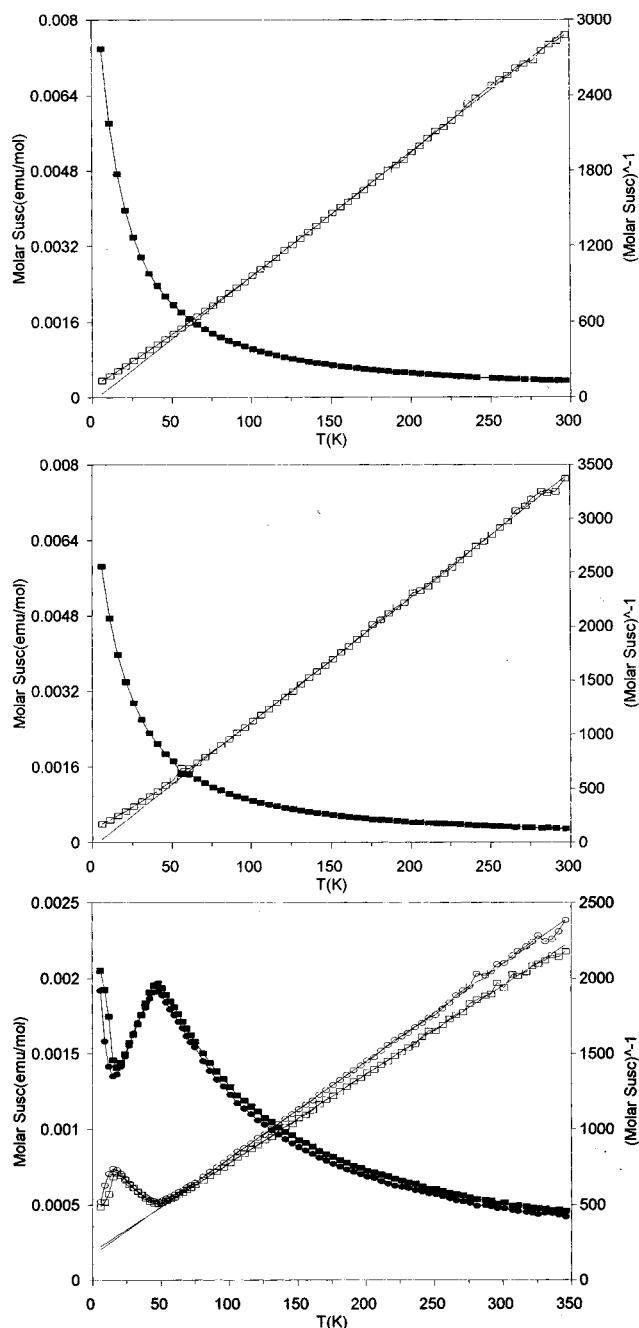

Figure 5. Nonlinear Curie−Weiss fits to observed magnetic susceptibility data at 3 T as a function of temperature (K) with $\chi - \chi_o$ as solid squares, $(\chi - \chi_o)^{-1}$ as open squares. Top: $Cs_2La_{10}I_{17}Ni_2$; middle: $Cs_2La_{10}I_{17}Os_2$; bottom: $La_{10}I_{15}Os_2$ (data measured at 1 T are shown as circles).

Table 7. Parameters That Fit the Molar Magnetic Susceptibilities of $Cs_2La_{10}I_{17}Z_2$, Z = Ni, Os, and $La_{10}I_{15}Os_2$ to $\chi = C/(T-\theta) + \chi_o$

compd	H (T)	range (K)	C	θ (K)	χ_o (10^{-4} emu mol^{-1})	μ (μ_B)
$Cs_2La_{10}I_{17}Ni_2$	3	100−300	0.101(2)	3(1)	9.59(7)	0.90(1)
$Cs_2La_{10}I_{17}Os_2$	3	100−300	0.086(2)	4(2)	6.60(6)	0.83(1)
$La_{10}I_{15}Os_2$	3	100−350	0.155(4)	−25(2)	7.06(9)	1.11(1)
	1	100−350	0.171(4)	−32(2)	6.90(8)	1.17(1)

function $\chi = C/(T - \theta) + \chi_o$ with the parameters listed in Table 7. The small θ parameters for the two $Cs_2La_{10}I_{17}Z_2$ (3, 4 K) as well as the fits of $1/(\chi - \chi_o)$ vs T in Figure 5a,b indicate fairly ideal paramagnetic behavior to quite low temperatures. On the other hand, intercluster magnetic coupling within the more tightly interbridged $La_{10}I_{15}Os_2$ seems to be evidenced by an

apparent antiferromagnetic transition at $T_c \sim 46$ K, Figure 5c, as well as the Weiss constant parameters of $-25(2)$ and $-32(2)$ K for data at 3 and 1 T, respectively. The shorter La5–La5 intercluster separations in the last along $\bar{b}$, 4.77 Å, as well as the nearby La5–La4 (4.94 Å) and La5–La2 (5.18 Å) distances, all generated by iodine bridging modes, are attractive coupling routes. Although these are not so different from the single 4.87 Å La2–La2 separations between clusters in $Cs_2La_{10}I_{17}Co_2$ (Figures 1 and 2), the latter are bridged by planar iodines which appear less effective in coupling. The χ_o valves for all three compounds are in a small range, 6.6×10^{-4} to 9.6×10^{-4} emu mol^{-1}. These are comparable to the 7.6×10^{-4} emu mol^{-1} per cluster similarly deduced for $La_{12}I_{17}Fe_2$, a heavily interbridged paramagnetic array of $La_6(Fe)I_{12}$-type clusters,[29] as well as those in a large number of other cluster halides of yttrium, zirconium, niobium, and tantalum cited in ref 9. We presume these χ_o values are all of the character of van Vleck, temperature-independent paramagnetism.

The focus of the magnetic investigations is of course the moments, which range from about 0.8 to 1.1 μ_B per dimer at 3 T (Table 7). These lie below the ideal spin-only value of 1.73 μ_B for one unpaired electron, but they are comparable to those for both the 17-electron monoclusters in $La_{12}I_{17}Fe_2$, 1.11 μ_B,[28] and the magnetically less well behaved $CsLa_6I_{10}Fe$, ca. 1.4 μ_B.[17] These differences might result from spin–orbital coupling with such heavy cluster elements, but the true origins of such deviations have never been established. Of course, weak antiferromagnetic coupling between clusters could contribute as well to the quenching of the magnetic moment, an effect clearly observed with $La_{10}I_{15}Os_2$. The room temperature resistivity of $Cs_2La_{10}I_{17}Co_2$ is above that which can be detected by our "Q" (high frequency, electrodeless) apparatus, which usually means greater than $800-1000$ $\mu\Omega\cdot$cm.

Bonding Calculations. Extended Hückel MO calculations were made first to compare the bonding within the ubiquitous R_6Z octahedral clusters with that in these new transition-metal-centered $R_{10}Z_2$ bioctahedral clusters, in each case with all edges and vertices appropriately bonded to iodine. Full EH band calculations were also carried out on the two structures to compare with the treatment of the more localized bonding in a molecular orbital sense, as the latter has been the practice for compounds containing discrete octahedral clusters. Both band calculations used the more reliable charge-iterated energy parameters for cobalt and lanthanum. Although only the osmium analog $La_{10}I_{15}Os_2$ is known in the ternary systems, other calculations using parameters reasonable for osmium did not significantly alter the band picture.

Calculations for the molecular cluster were performed for an idealized $La_{10}I_{18}Co_2$ cluster with D_{2h} point symmetry oriented such that the shared edge lay along the y axis and the two Co atoms were located on the x axis. As before, each cluster was not only edge-bridged by iodine but also sheathed in extra iodine atoms at all exo positions, which are important interactions that lie trans to the apical R–Z bonding. The molecular orbital diagrams for the metal-based orbitals of the corresponding monomeric cluster unit $La_6I_{18}Co^{6-}$ and the dimeric $La_{10}I_{26}Co_2^{11-}$ are shown in Figure 6. All orbitals in the latter are nondegenerate in this lower symmetry. The bonding within the biocta-hedral cluster is qualitatively similar to that of the component octahedral clusters. Two La–Z σ-bonding orbitals are located at the bottom of the group followed by the La–Z π-bonding orbitals. There are only four π-orbitals because of the edge-sharing nature of the cluster. Condensation at one cluster edge
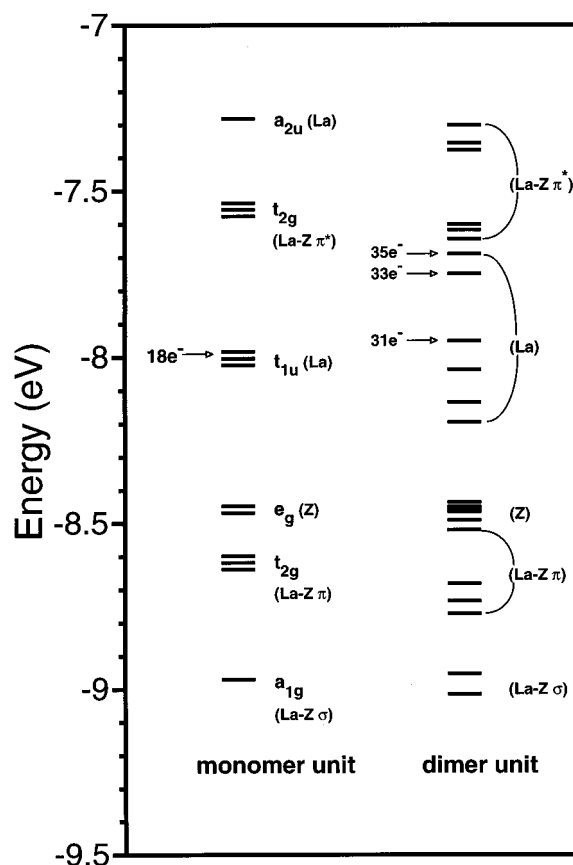
(29) Payne, M. W.; Dorhout P. K.; Corbett, J. D. *Inorg. Chem.* **1991**, *31*, 1389.

Figure 6. Comparative extended-Hückel calculations: (left) the single octahedral $(La_6I_{12}Co)I_6^{6-}$; (right) the D_{2h} bioctahedral $(La_{10}I_{18}Co_2)I_8^{11-}$ cluster. Atom contributions are marked. The $31e^-$, $33e^-$, and $35e^-$ labels mark half-filled HOMO levels for Z = Ru or Os, Co, and Ni, respectively.

means the loss of two of the six La-based former t_{2g} orbitals on the octahedra, orbitals that would be retained if the two clusters were instead interconnected by two additional La–La bonds. The next six orbitals are the nonbonding interstitial (Z) orbitals. Four of these are the two e_g nonbonding sets from the octahedral components, while the other two orbitals are the left-over interstitial-based t_{2g} orbitals (above) that no longer participate in the La–Z π-bonding. (Four orbitals lie in what reproduces in the figure as a solid bar.)

The next group of orbitals above the nonbonding d-orbitals on Z are the La–La intracluster bonding orbitals around -8 eV that originate with the t_{1u} La-based orbitals in the mono-cluster. The first four are σ- and π-bonding orbitals among the six La atoms in the waist of the bicluster. The next two orbitals, the HOMOs for 33- and 35-electron clusters, are more weakly bonding orbitals on the four La apex atoms. The splitting among these in the process of dimerization becomes quite significant. Fusion of the two octahedral clusters into the bioctahedral cluster has a much larger effect on the La-based orbitals than on those involving the relatively isolated intersti-tials. The splitting of the former t_{1u} sets is the same kind as seen when building a one-dimensional chain one atom at a time: each new atom on the chain produces a slightly wider splitting (band). The bioctahedral cluster is thus the first step to producing a one-dimensional chain as found in Pr_4I_5Ru.[29]

The group of orbitals that lie just above the HOMOs for the highest observed electron count are La–Z π^* orbitals. This would suggest that 35 (or 36) cluster-based electrons could be the maximal count for the bioctahedral cluster. However, in the three-dimensional solids, the results for more condensed solid $La_{10}I_{15}Os_2$ (below) show more significant filling of the

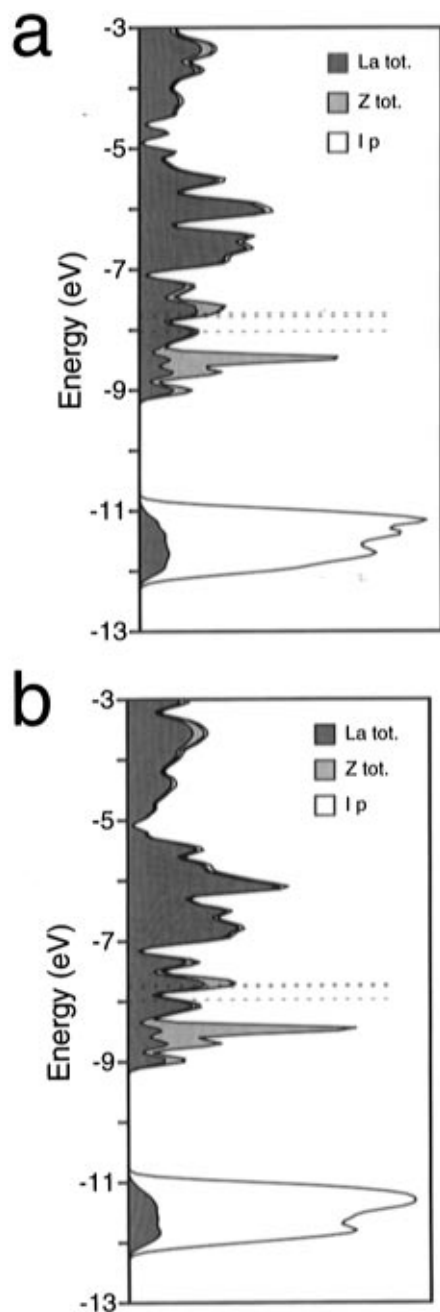**Figure 7.** Densities-of-states as a function of energy from band calculations for (a) $La_{10}I_{17}Co_2^{2-}$ and (b) $La_{10}I_{15}Co_2$, with atom contributions shaded. The dashed lines correspond to Fermi energies of 31 (Z = Ru, Os), 33 (Co), and 35 (Ni) electrons.

La−Z π^* for electron counts of 33 and 35 than in the less condensed $Cs_2R_{10}I_{17}Z_2$ compounds. The filling of these anti-bonding orbitals may be a major factor that limits interstitial variations of the $La_{10}I_{15}Os_2$ structure. Insertion of Co, Ni, Rh, etc. did not succeed, but of course there are many reasons why the synthesis of electronically reasonable compounds may fail, most particularly because of the stability of alternate phases.

The densities-of-states (DOS) summaries of what are a collection of quite flat bands in k-space are shown in Figure 7 for (a) $La_{10}I_{17}Co_2^{2-}$ and (b) $La_{10}I_{15}Co_2$. The main features of the DOS for both structures are similar, as was expected since the primary difference between the two structures is the connectivity between clusters not the bioctahedral clusters themselves. The large energy band (peak) in DOS centered around −11 eV is largely comprised of I p orbitals plus a significant contribution from the La d, the latter arising from

the covalent nature of the La−I bonding. The next peak starting around −9.25 eV originates in both cases from orbitals of the rare-earth metal and the interstitial, largely 5d and 3d, respectively, with states near the bottom of this band being primarily interstitial d and s orbitals. The locations of the interstitial orbitals are naturally dependent on the H_{ii} values utilized, but the earlier band calculations on the centered cluster iodides in $Y_6I_{10}Ru$[5] and the one-dimensional condensed chain structure of Pr_4I_5Ru[29] with charge-iterated parameters also placed the major interstitial contributions in a fairly narrow region below the Fermi energy. This is consistent as well with the relative electronegativities or d ionization energies of R and Z. The three Fermi energies marked on the DOS plots correspond to those for the three types of interstitials found in the $Cs_2R_{10}I_{17}Z_2$ structure type: 31 cluster-based electrons for Os or Ru, 33 for Co, and 35 with Ni. The orbital contributions near or just below these Fermi energies are for La−La intracluster bonding. There is a growing contribution from interstitial d orbitals at the higher Fermi levels. This effect is greater in the $La_{10}I_{15}Os_2$ structure, which is presently known only with 31 electrons per bicluster.

Comparison of Figures 6 and 7 shows that the filled metal-based molecular orbitals of the bioctahedral cluster map onto the four peaks in the DOS plot above −9.5 eV quite well, as has been the case for other halide cluster systems. This is as expected when the metal−metal bonding interactions are very largely intracluster, and the individual bands in k-space are quite flat. Minor intercluster interactions are also reflected in the low temperature coupling of localized spins seen in the magnetic properties of $La_{15}I_{17}Os_2$. The DOS results are in this sense misleading; the compounds are far from the metallic states suggested by the gross features of a Fermi energy cutting large bands. Rather, the individual bands lack significant dispersion, the spin states are localized, and the compounds are at best semiconducting. The breakdown of band theory is legendary when electron exchange and correlation become large relative to width of the individual bands, giving what is often called a Mott insulator. Calculations showing this are well beyond the simple Hückel methodology.

The compounds reported here are the first examples both of metal biclusters centered by transition metals and of intermediates between isolated R_6-type clusters and infinite chains of condensed metal-centered clusters in related systems. The ternary $La_{10}I_{15}Os_2$ compound necessarily exhibits more intercluster iodine bridging than does $Cs_2La_{10}I_{17}Os_2$, etc., and the means by which the otherwise similar structures may be interconverted with CsI is readily visualized. EHMO calculations give an adequate description of localized bonding in the bicluster phases, all of which have an odd number of skeletal electrons, as demonstrated by magnetic data for three. The corresponding EH band calculation results present an unrealistic open-band picture for the compounds by neglecting the consequences of very narrow bands and electron correlation.

Supporting Information Available: Tables of detailed data collection and refinement information and anisotropic displacement parameters for the atoms in $Cs_2Ce_{10}I_{17}Os_2$ and $La_{10}I_{15}Os_2$ (3 pages). See any current masthead page for ordering information and Internet access instructions.

JA9630607